Local surrogate responses in the Schwarz alternating method for elastic problems on random voided domains

Martin Drieschner[1], Robert Gruhlke[2],

Yuri Petryna[1], Martin Eigel[2], Dietmar Hömberg[2,3,4]

submitted: March 28, 2022

[1] Technische Universität Berlin
Department of Civil Engineering, Chair of Structural Mechanics
Gustav-Meyer-Allee 25
13355 Berlin
Germany
E-Mail: martin.drieschner@tu-berlin.de
         yuriy.petryna@tu-berlin.de

[2] Weierstrass Institute
Mohrenstr. 39
10117 Berlin
Germany
E-Mail: robert.gruhlke@wias-berlin.de
         martin.eigel@wias-berlin.de
         dietmar.hoemberg@wias-berlin.de

[3] Department of
Mathematical Sciences
NTNU
Alfred Getz vei 1
7491 Trondheim
Norway

[4] Technische Universität Berlin
Institut für Mathematik
Str. des 17. Juni 136
10623 Berlin
Germany

No. 2928

Berlin 2022

Local surrogate responses in the Schwarz alternating method for elastic problems on random voided domains

Martin Drieschner, Robert Gruhlke,
Yuri Petryna, Martin Eigel, Dietmar Hömberg

Abstract

Imperfections and inaccuracies in real technical products often influence the mechanical behavior and the overall structural reliability. The prediction of real stress states and possibly resulting failure mechanisms is essential and a real challenge, e.g. in the design process. In this contribution, imperfections in elastic materials such as air voids in adhesive bonds between fiber-reinforced composites are investigated. They are modeled as arbitrarily shaped and positioned. The focus is on local displacement values as well as on associated stress concentrations caused by the imperfections. For this purpose, the resulting complex random one-scale finite element model is numerically solved by a new developed surrogate model using an overlapping domain decomposition scheme based on Schwarz alternating method. Here, the actual response of local subproblems associated with isolated material imperfections is determined by a single appropriate surrogate model, that allows for an accelerated propagation of randomness. The efficiency of the method is demonstrated for imperfections with elliptical and ellipsoidal shape in 2D and 3D and extended to arbitrarily shaped voids. For the latter one, a local surrogate model based on artificial neural networks (ANN) is constructed. Finally, a comparison to experimental results validates the numerical predictions for a real engineering problem.

1   Introduction

Stress concentrations in engineering structures can initiate local cracking with a following crack propagation through the structure, and at worst, lead to global structural failure [1, 28]. Such phenomena can be observed due to geometrical or material discontinuities. Therefore, it is necessary to investigate in detail the influence of such imperfections, inaccuracies and inhomogeneities on the overall system behavior. In general, air voids resulting from manufacturing processes or environmental conditions are unavoidable in many different materials like asphalt mixtures [19], die-cast ZAMAK [17], epoxy resin [15], mortar or concrete [13]. In [23], an extensive overview with a broad spectrum of numerical investigations of holes in plates is given. Experiments on holed structures can be found in the literature, e.g. in [16] where the shear failure behavior of lipped channel beams have been studied. The experiments have indicated that the main factor influencing the strength is the ratio of the depth of web openings to the clear height of the web. Yielding and buckling of plate girders with perforated webs under axial compression and bending moment have been investigated in [27]. The influence of the hole location on the ultimate load capacity has been verified experimentally and numerically. Sometimes, the air void properties like amount, size, position and shape are uncertain or vaguely detectable by non-destructive testing (NDT) like in adhesive bonds of rotor blades of wind turbines [22]. For this, some studies have already been done by the authors, see [18, 7, 6, 10]. Motivated by the presence of air voids in diverse engineering applications, this work sets its focus to efficient numerical simulations of linear elastic materials with random voids.

The challenge in the numerical simulations of these type of problems lies in the fact that the solutions contains many multiscale features and thus require very fine meshes to resolve them. Such problems have been investigated in the deterministic setting using reduced basis and generalized multiscale finite element methods, exemplarily in [3, 4].

In the setting of random domains containing a random number of voids parametrized by random parameters, two main challenges arise. The first challenge is introduced by the possible unknown correlation structure of the random input variables. The second challenge is caused by the possible high-dimensional parameter space. Both aspects may not allow a straightforward application of surrogate models leading to the application of sampling approaches.

Motivated by the application in mind detecting local behavior such as stress concentrations, a combined technique is developed in this work based on global sampling and local surrogate techniques. Here, the main idea is to propagate uncertainty in a substructuring framework based on localized random dependence. Such ideas have been applied successfully in the context of partial differential equations with random coefficients in the smooth case using Schur complement formalism [5] and in the non-smooth case including composite materials in [11] based on FETI-DP. These techniques are extended to the case of random domains, locally allowing for non-matching meshes in a formalism of overlapping substructuring methods based on the Schwarz alternating method [25]. This approach allows for fine meshes around the local features, while using a moderately sized discretization of the remaining domain.

Surrogates are trained in an offline phase and replace the system response of a neighbored area of an isolated void. Hence, no meshing, assembling and solving in the neighborhood of material imperfections is required in the online phase. Consequently, the idea can be interpreted as an effective reduction of degrees of freedom in the remaining domain and yields an accelerated propagation of uncertainty. The developed method combines the advantages from both worlds: Sampling to circumvent the curse of dimensionality and surrogate techniques for the fast propagation of uncertainty without the need of additional numerical computation in the online phase.

The accelerated scheme is then applied on linear elastostatic problems defined on domains with isotropic material and star-shaped voids in 2D and 3D, with the special case of elliptical and ellipsoidal shapes.

The remainder of this paper is organized as follows: Section 2 provides the linear elastostatic boundary value problem for two- and three-dimensional holed structures. The Schwarz alternating method to decompose the model and the local problems having localized uncertainty in the subdomain are described in Section 3. Strategies for the surrogate response of the problem formulation are presented in Section 4. The application of the presented models on three examples is given in Section 5. The solutions of the proposed surrogate modeling approaches are compared with those of the one-scale model. Furthermore, experimentally determined strains are used for validation of the numerical methods. Finally, some concluding remarks and an outlook on the ongoing work are given in Section 6.

2   Parametric elastostatic model for holed domains

This Section 2 is devoted to the description of the linear elastostatic model equation on random domains. The focus is on the prediction of displacements and principal stresses in the neighborhood of material imperfections modeled by random voids.

2.1 Model of random voids

Let $(\Omega, \sigma, \mathbb{P})$ be a random space. Let $\hat{D} \subset \mathbb{R}^d$, $d = \{2, 3\}$, be a reference body which is occupied by a random number $N = N(\omega) \in \mathbb{N}$ of random holed structures

$$\mathcal{P}(\omega) = \{P_k(\omega), k = 1, \ldots, N\} \subset \hat{D}, \quad \omega \in \Omega, \tag{1}$$

yielding a holed LIPSCHITZ domain $D(\omega) = \hat{D} \backslash \mathcal{P}(\omega)$. It is assumed that the random dependency of the voids $P_k(\omega) \in \mathcal{P}(\omega)$ is encoded by a random vector $\boldsymbol{\xi}(\omega) = (\xi_1(\omega), \ldots, \xi_N(\omega))$ with $\xi_k(\omega) \colon \Omega \to \Xi_k \subset \Xi_0 \subset \mathbb{R}^{M_k < \infty}$ such that $P_k(\omega) = P(\xi_k(\omega))$ for $k = 1, \ldots, N$ with a joint distribution of $\boldsymbol{\xi}$ from which samples can be drawn. In general $\mathrm{img}\,\boldsymbol{\xi} =: \Xi \subset \times_{k=1}^{N} \Xi_k$ with strict inclusion, for example in the case, when the random voids are correlated by geometric constraints. In what follows, the notations of parameter identification $\boldsymbol{p} = \boldsymbol{\xi}(\omega) \in \Gamma$ and $\boldsymbol{p}_k = \xi_k(\omega)$ are used. Note that the case of periodic perforations is included for which the parameterization may be simplified, using global parameters for distance and size only.

In the application in mind, each void is elliptical/ ellipsoidal or star-shaped. The latter structures are generated by the choice of a random vantage point and a finite number of random radii in preselected angular directions. Trigonometric interpolation is then applied in radial direction to obtain a continuous model of the void. Since the presented approach relies on the use of local coordinate systems associated to each P_k, its parameterization $\boldsymbol{p}_k$ does not contain midpoint or vantage point information. In the case of elliptical/ ellipsoidal voids, $\boldsymbol{p}_k \in \mathbb{R}^d$ only corresponds to radii whereas $\boldsymbol{p}_k \in \mathbb{R}^{M_k}$ is a vector of M_k radii associated to predetermined angles in an associated local polar coordinate system for star-shaped voids.

2.2 Random model equation

Consider a linear elastostatic boundary value problem of the form

$$
\left.
\begin{aligned}
\boldsymbol{f}(\omega) &= -\operatorname{div}\boldsymbol{\sigma} && \text{equilibrium eq.} \\
\boldsymbol{\epsilon} &= \left[\nabla\boldsymbol{u} + \nabla^{\mathrm{T}}\boldsymbol{u}\right]/2 && \text{strain-displacement eq.} \\
\boldsymbol{\sigma} &= \boldsymbol{C} : \boldsymbol{\epsilon} && \text{constitutive eq.}
\end{aligned}
\right\} \quad \text{in } D(\omega),
$$
$$
\begin{aligned}
\boldsymbol{u} &= \boldsymbol{0} && \text{Dirichlet b.c.} && \text{on } \Gamma_{\boldsymbol{0}}, \\
\boldsymbol{\sigma} \cdot \boldsymbol{n} &= \boldsymbol{g}(\omega) && \text{Neumann b.c.} && \text{on } \Gamma_{\boldsymbol{\sigma}}, \\
\boldsymbol{\sigma} \cdot \boldsymbol{n} &= \boldsymbol{0} && \text{Neumann b.c.} && \text{on } \Gamma_{\boldsymbol{\sigma},\boldsymbol{0}}(\omega),
\end{aligned}
\tag{2}
$$

with deterministic disjoint boundary segments $\Gamma_{\boldsymbol{0}}, \Gamma_{\boldsymbol{\sigma}} \subset \partial\hat{D}$ with $\partial\hat{D} = \Gamma_{\boldsymbol{0}} \cup \Gamma_{\boldsymbol{\sigma}}$, $|\Gamma_{\boldsymbol{0}}| > 0$ and a realization of the void boundary $\Gamma_{\boldsymbol{\sigma},\boldsymbol{0}}(\omega) := \partial\left(\bigcup_{P \in \mathcal{P}(\omega)} P\right)$. Note that the case of random holed structures intersecting with the boundary of $\hat{D}$ has been excluded since $\Gamma_{\boldsymbol{0}}$ and $\Gamma_{\boldsymbol{\sigma}}$ are assumed to be deterministic. Let the random data $\boldsymbol{C}$, $\boldsymbol{f}(\omega)$ and $\boldsymbol{g}(\omega)$ be regular enough in $\boldsymbol{x} \in D(\omega)$ such that the LAX-MILGRAM theorem applies to ensure existence and uniqueness of a (weak) pointwise solution $\boldsymbol{u}(\omega) \in V := H^1_{\Gamma_{\boldsymbol{0}}}(D(\omega))^d$ solving the variational formulation for almost all $\omega \in \Omega$

$$\int_{D(\omega)} \boldsymbol{\sigma}(\boldsymbol{u}) : \boldsymbol{\epsilon}(\boldsymbol{v})\,\mathrm{d}\boldsymbol{x} = \int_{D(\omega)} \boldsymbol{f}(\omega) \cdot \boldsymbol{v}\,\mathrm{d}\boldsymbol{x} + \int_{\Gamma_\sigma} \boldsymbol{g}(\omega) \cdot \boldsymbol{v}\mathrm{d}\mathrm{S}, \quad \text{for all } \boldsymbol{v} \in V. \tag{3}$$

For the applications in Section 5, the reference body $\hat{D}$ is a rectangle $(L \times W)$ for $d = 2$ or a cuboid $(L \times W \times T)$ for $d = 3$, respectively. Furthermore, $\boldsymbol{f}(\omega)$ is modeled as $\boldsymbol{f} \equiv 0$ and the

deterministic material response C is given as $C = \lambda I_2 \otimes I_2 + 2\mu I_4$ with second- and forth-order identity tensors I_2 and I_4. The LAMÉ constants $\lambda = E\nu/[(1+\nu)(1-2\nu)]$ and $\mu = E/[2(1+\nu)]$ with given YOUNG's modulus E and POISSON's ratio ν describe isotropic material. Holed domains are exemplarily illustrated in Fig. 1.

(a) Arbitrarily shaped voids in 2D

(b) Ellipsoidal voids in 3D
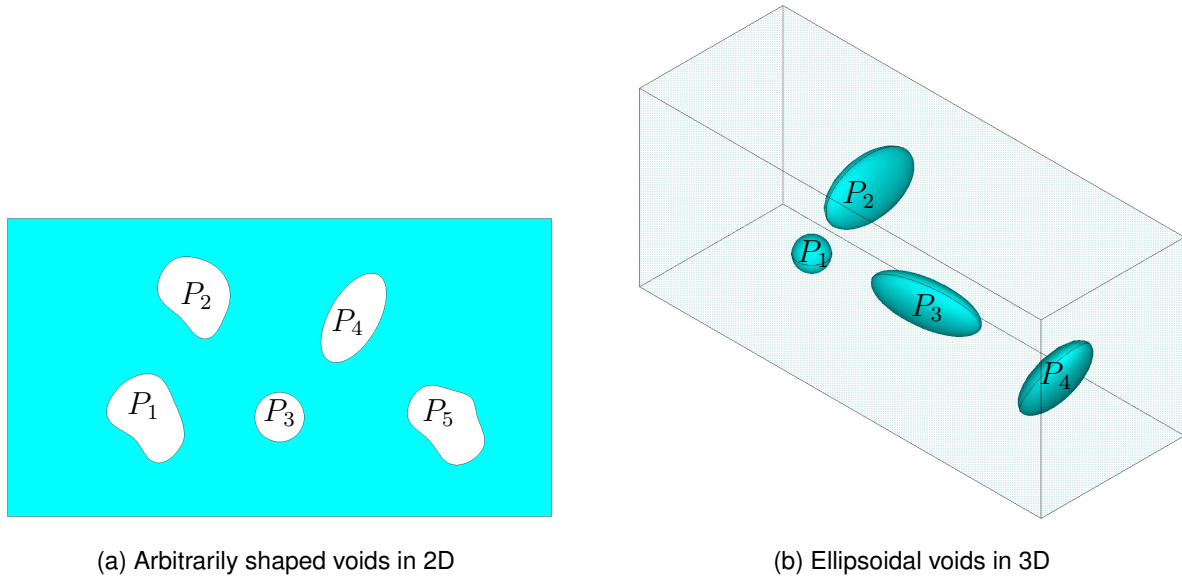
Figure 1: Schematic holed domain $D(\omega)$ according to Eq. (2).

2.3 Quantities of interest

The general objective is to predict the displacement field $u(x)$ in the overall holed domain $D(\omega)$. Furthermore, stress concentrations around the included voids $P_k(\omega)$ are often of interest for practical issues, e.g. for a qualitative and quantitative comparison with experimentally determined failure mechanisms and ultimate loads [10]. The maximum first principal stress and the minimum third principal stress are to be determined:

$$\sigma_{1,\max} = \sigma_{1,\max}(\omega) = \operatorname*{ess\,sup}_{x \in D(\omega)} \lambda_{\max}(\boldsymbol{\sigma}(\boldsymbol{u})[\boldsymbol{x}]), \tag{4}$$

$$\sigma_{3,\min} = \sigma_{3,\min}(\omega) = \operatorname*{ess\,inf}_{x \in D(\omega)} \lambda_{\min}(\boldsymbol{\sigma}(\boldsymbol{u})[\boldsymbol{x}]). \tag{5}$$

Here $\lambda_{\max}(A)$ and $\lambda_{\min}(A)$ denote the largest and smallest eigenvalue of a matrix A, respectively. Finally, in the practical example in Section 5.3, the axial strains ϵ_x have to be measured which can easily calculated from the displacement field by

$$\epsilon_x = \epsilon_x(\boldsymbol{x}) = \frac{\partial}{\partial x} u_x(\boldsymbol{x}). \tag{6}$$

3 Local surrogate based on substructuring and random voids

In this Section 3, the proposed method to solve the linear elastostatic problem in Eq. (2) in the presence of random voids in an accelerated sampling framework is presented. The acceleration is based on the
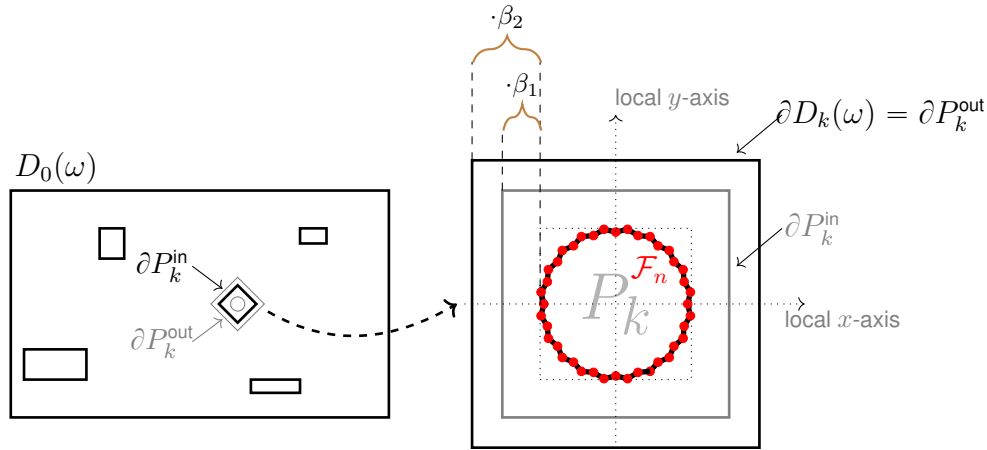
Figure 2: Schematic domain decomposition. **Left**: Domain $D_0(\omega)$ with rectangular cutouts $\mathcal{P}^{\text{in}}(\omega)$. **Right**: Subdomain $D_k(\omega)$ with void $P_k(\omega)$ and surrounding domains $\{P_k^{\text{in}}(\omega), P_k^{\text{out}}(\omega)\}$ based on relative values $\{\beta_1, \beta_2\}$ in the local coordinate system.

Schwarz alternating method, which is an overlapping substructuring method, where the response of the subproblems associated with the random voids is substituted by suitable surrogate models. The Schwarz alternating method allows to use independent and possible non-matching meshes. Consequently, while local subproblems based on fine meshes do not cause additional computational effort by using the surrogate response, the workload is determined by the iteration number and the computation of the system defined on the remaining domain.

3.1 Schwarz alternating method

When approximating a solution of a real problem by using the finite element method (FEM), the accuracy mainly depends on the quality and size of the mesh on the one hand (h-convergence) and the degree of the underlying shape functions within the elements on the other hand (p-convergence). In the presence of geometric details, such as the arbitrarily shaped voids in mind, a necessary fine mesh resolution significantly increases the workload of the associated FEM computation. In particular as the mesh sizes decrease, the condition number of the associated algebraic systems grows and encourages the need of so called preconditioning. A popular class of preconditioners is based on substructuring or domain decomposition techniques [26], which is the underlying approach of choice for the introduced method. The technique developed in this contribution is based on the overlapping Schwarz alternating method [25].

Let $\omega \in \Omega$ and recall our random domain of interest $D(\omega)$ resulting from a set of random holed structures $\mathcal{P}(\omega)$. Assume that there exist sets of simpler geometries

$$\mathcal{P}^{\#}(\omega) = \{P_1^{\#}(\omega), \ldots, P_N^{\#}(\omega)\}, \quad \text{with } \# \in \{\text{in,out}\}, \tag{7}$$

such that $P_k(\omega) \subset P_k^{\text{in}}(\omega) \subset P_k^{\text{out}}(\omega)$ with $P_k^{\text{out}}(\omega) \cap P_{k'}^{\text{out}}(\omega) = \varnothing$ if $k \neq k'$. Furthermore, define the domain as $D_0(\omega) := \hat{D}\backslash\mathcal{P}^{\text{in}}(\omega)$ and the subdomains as $D_k(\omega) := P_k^{\text{out}}(\omega)$ for $k = 1, \ldots, N$, see Fig. 2. The terminology "simpler geometry" is motivated by a reduced workload due to the domain $D_0(\omega)$ even if quantities of interest associated to the random structures within the subdomains $D_k(\omega)$ are of particular importance, such as local stress concentrations. Then, Eq. (2) is reformulated for

$\cdot_k = \cdot|_{D_k}$ as

$$\left.\begin{array}{rcl} \boldsymbol{f}(\omega) & = & -\operatorname{div}\boldsymbol{\sigma}_k \\ \boldsymbol{\epsilon}_k & = & \left[\nabla\boldsymbol{u}_k + \nabla^{\mathrm{T}}\boldsymbol{u}_k\right]/2 \\ \boldsymbol{\sigma}_k & = & \boldsymbol{C}:\boldsymbol{\epsilon}_k \end{array}\right\} \quad \text{in } D_k(\omega) \text{ for } k = 1,\ldots,N \tag{8}$$

with coupling by Dirichlet boundary conditions for $k = 1,\ldots,N$ such that

$$\begin{cases} \boldsymbol{u}_0 & = & \boldsymbol{0} & \text{on } \Gamma_{\boldsymbol{0}}, \\ \boldsymbol{\sigma}_0\cdot\boldsymbol{n} & = & \boldsymbol{g}(\omega) & \text{on } \Gamma_{\boldsymbol{\sigma}}, \\ \boldsymbol{u}_0 & = & \boldsymbol{u}_k & \text{on } \partial P_k^{\text{in}}(\omega), \end{cases} \qquad \begin{cases} \boldsymbol{\sigma}_k\cdot\boldsymbol{n} & = & \boldsymbol{0} & \text{on } \partial P_k(\omega), \\ \boldsymbol{u}_k & = & \boldsymbol{u}_0 & \text{on } \partial P_k^{\text{out}}(\omega). \end{cases} \tag{9}$$

Alternating iterations between these equations given an initial Dirichlet trace until convergence are then conducted in the classical Schwarz alternating method.

3.2 Local subproblems

The Eqs. (8)–(9) in the subdomain $D_k(\omega)$ for $k > 0$ associated with a single void $P_k(\omega)$ are investigated in the following, especially the need of accurate mesh resolutions. Furthermore, a family of parametrized meshes within the discretization process itself is presented. This approach is essential to enable suitable surrogate response techniques in Section 4.

3.2.1 Mesh resolution and accuracy

For illustration, the void P_1 of Fig. 1 has been separated and investigated briefly. Uniaxial tension has been applied in horizontal direction. The maximum first principal and the minimum third principal stress using Eqs. (4)–(5) have been calculated for different amounts of elements on the boundaries $\partial P_1^{\text{out}}$ (here with rectangular shape) and ∂P_1, respectively. It has been determined that a relatively high amount of elements on ∂P_1 should be used, at least 120. Also the amount of elements on $\partial P_1^{\text{out}}$ influences the stress values, leading in total to a high amount of degrees of freedom for an accurate prediction of local stress concentrations, see Fig. 3. As a compromise between efficiency and accuracy, the configuration with 40 elements on ∂D_k and 360 elements on ∂P_k has been used in the following. Furthermore, a layer with nearly square-shaped elements has been added around the void to increase the accuracy of the stress prediction on the voids, see also Fig. 3.

3.2.2 Parameter model

Given the structure of the random voids, in particular the parameter dependence of an isolated P_k from $\boldsymbol{p}_k$, the construction of a single parameter dependent model is envisaged. Then, this model can replace, over the loop of sample realizations, the response of any subproblem within Eqs. (8)–(9) for $k = 1,\ldots,N$. Geometries P_k^{in} and P_k^{out} of possibly rotated rectangular ($d = 2$) or cuboid ($d = 3$) shape are considered, which are aligned with the void in a local coordinate system and sized by fixed relative ratios $\beta_2 > \beta_1 > 0$, see Fig. 2. Throughout the iterative process within the Schwarz alternating method, the local problems on $D_k(\omega) = P_k^{\text{out}}(\omega)$ with void P_k depending on $\boldsymbol{p}_k$ only differ by a change of the Dirichlet boundary condition on $\partial D_k(\omega)$.

Finally, let $\mathcal{S}(\boldsymbol{p}_k)$ denote the corresponding linear solution operator, mapping the current Dirichlet trace to the local solution.

(a) Maximum first principal stress

(b) Minimum third principal stress
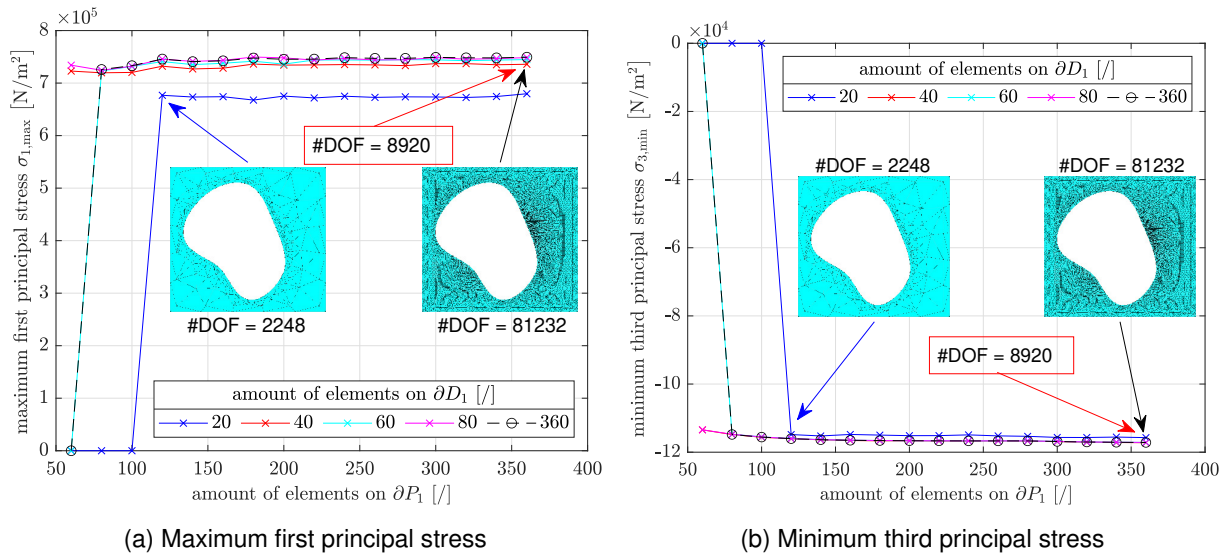
Figure 3: Stress convergence plots for the subdomain D_1 with outer boundary $\partial D_1 = \partial P_1^{\text{out}}$ and an arbitrarily shaped void P_1 with boundary ∂P_1.

3.2.3 Smooth parameter dependent family of discretization

Motivated by Section 3.2.1, a fixed mesh discretization scheme is used for a fixed range of parameters $\boldsymbol{p}_k$. Let $\Xi_0 = \bigcup_{\ell=1}^{L} \Xi_0^\ell$, $L \in \mathbb{N}$, be a disjoint partition of the local hold all domain Ξ_0 defined in Section 2.1.

For fixed $\ell = 1, \dots, L$, any subdomain $D_k = P_k^{\text{out}}$ with void $P_k = P_k(\boldsymbol{p}_k)$ for $\boldsymbol{p}_k \in \Xi^\ell$ is discretized by a mesh $\mathcal{M}_\ell = \mathcal{M}_\ell(\boldsymbol{p}_k)$ such that:

1 There are $N_\ell \in \mathbb{N}$ vertices on ∂P_k.

2 There are $N_{\ell,x_i} \in \mathbb{N}$, $i = 1, \dots, d$ equidistantly distributed vertices on ∂P_k^{in} and $\partial P_k^{\text{out}}$.

3 The mesh $\mathcal{M}_\ell(\boldsymbol{p}_k)$ of $P_k^{\text{out}} \backslash P_k$ is the result of a reference mesh $\hat{M}_\ell$ with reference void $\hat{P}_\ell$ and surrounding reference rectangles/ cuboids $\{\hat{P}_\ell^{\text{in}}, \hat{P}_\ell^{\text{out}}\}$ under a smooth mapping Ψ_ℓ, such that $\Psi_\ell(\hat{M}_\ell, \boldsymbol{p}_k) = \mathcal{M}_\ell(\boldsymbol{p}_k)$.

Automatic mesh generators are restricted to the first two rules and consequently introduce a non-continuous parametric family of meshes in the sense that computations based on these meshes lead to non-continuous trajectories with regard to $\boldsymbol{p}_k$, see Fig. 4 for a counter example. Fortunately, this issue is resolved by the smooth mesh transformation Ψ_ℓ. The consequences of this construction are illustrated in Fig. 4 yielding piecewise continuous trajectories based on the partition using different reference meshes.

3.2.4 Explicit construction of Ψ for $d = 2$

An explicit construction of a smooth mesh transformation Ψ is exemplarily described for $d = 2$ in the following. Note that since P_k^{out} and P_k^{in} are (rotated) rectangles, there exists an affine map that transforms $D_k(\omega)$ in such a way that P_k^{in} gets mapped onto $[-1, 1]^2$. Let $\hat{\mathcal{M}}$ be a reference mesh defined on $[-1, 1]^2 \backslash \hat{P}$ with a reference star-shaped void $\hat{P}$ and let $P \subset [-1, 1]^2$ be a target star-shaped void, both having $\boldsymbol{0}$ as midpoint such that $B_{R_{\text{min}}}(\boldsymbol{0}) \subset \hat{P}, P \subset B_{R_{\text{max}}}(\boldsymbol{0})$, $0 < R_{\text{min}} <$
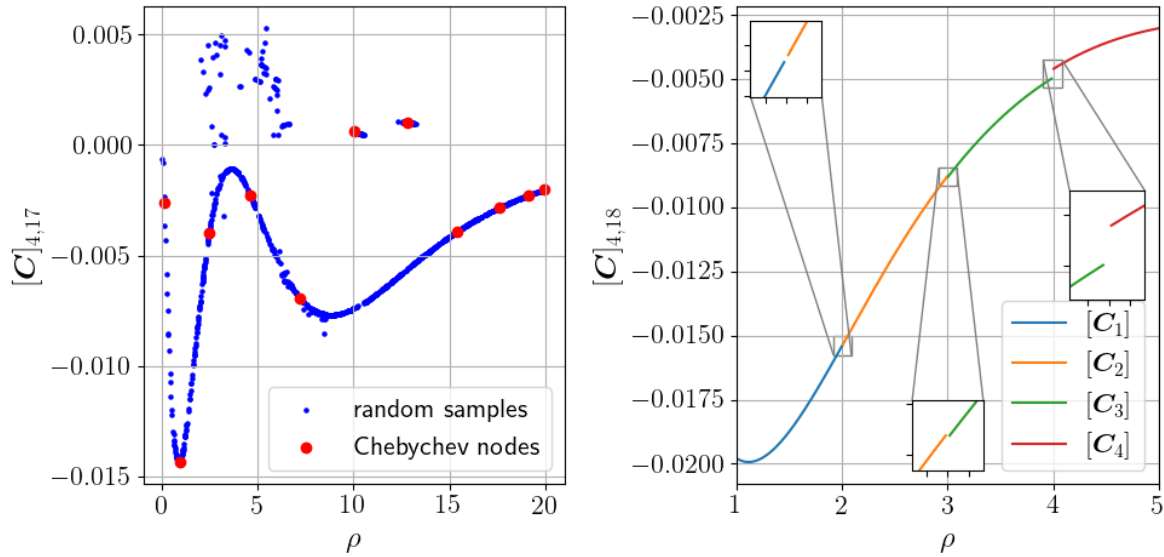
Figure 4: A simple elliptical void parametrized by ratio parameter $\rho = r_2/r_1$ as in Section 4.2.1 is meshed using a fixed amount of points on the inner and outer boundary. For $\boldsymbol{q}^{\text{in}} = \boldsymbol{q}^{\text{out}} = (4, 4, 4, 4)$. Two trajectories from entries of the matrix representation $\boldsymbol{C}_\ell$ in Eq. (14) of the compressed operator $\mathcal{C}_\ell$ from Eq. (13) are plotted. **Left**: Example trajectory using underlying automatic mesh generation, demonstrating lack of continuity. **Right:** Using different reference meshes $\hat{\mathcal{M}}_\ell$ for $\ell = 1, 2, 3, 4$ for a partition $\Xi_0 = [1, 2] \cup [2, 3] \cup [3, 4] \cup [4, 5]$, the transformation Ψ_ℓ yields piecewise smooth trajectories with controlled discontinuities with respect to the partition of Ξ_0.

$R_{\max} < 1$. Let $\theta \to \hat{\mathcal{F}}(\theta)$ and $\theta \to \mathcal{F}(\theta)$ denote a parameterization of the boundary of $\hat{P}$ and P respectively in local polar coordinates. Furthermore, define $\hat{\mathcal{F}}_n := \{\hat{\mathcal{F}}(2\pi i/n), i = 0, \ldots, n-1\}$ and $\mathcal{F}_n := \{\mathcal{F}(2\pi i/n), i = 0, \ldots, n-1\}$ for $n \in \mathbb{N}$. Assume that $\hat{\mathcal{F}}_n$ are the vertices of the reference void $\hat{P}$ in $\hat{\mathcal{M}}$ and consider the virtual points $\hat{\mathcal{F}}_{2n}$ and $\mathcal{F}_{2n}$. Then the transformation

$$\Psi(\hat{x}, \mathcal{F}_{2n}) = \sum_{i=1}^{2n} \chi_i(\hat{r})\phi_i(\hat{\theta}), \quad \hat{x} = \hat{r}[\cos\hat{\theta}, \sin\hat{\theta}]^T \tag{10}$$

with $\{\phi_i\}$ forms a smooth partition of unity of $[0, 2\pi]$ with $\phi_i(i\pi/n) = 1, \operatorname{supp}\phi_i = [(i-1)\pi/n, (i+1)\pi/n]$ and splines $\chi_i \in \mathcal{C}^k[0, \sqrt{2}]$ for $k \geqslant 2$. The spline χ_i is a strong monotonic interpolation polynomial with $\chi_i(|\hat{\mathcal{F}}(i\pi/n)|) = |\mathcal{F}(i\pi/n)|$ with input and output being radial components in the local coordinate system. Furthermore, χ_i coincides with the identity outside of $[R_{\min}, R_{\max}]$. Then, apart from forward and backward affine rescalings of $[-1, 1]^2$ and $D_k(\omega)$, Ψ of Eq. (10) can be used as underlying parameter depending transformation by noting the relation of parameter $\boldsymbol{p}_k$ to $\mathcal{F}_{2n}$. In Fig. 5, the construction based on different reference meshes corresponding to elliptical voids with different ratios is depicted.

4   Surrogate strategies for local subdomains

Based on the fixed mesh design of the local subproblems described in the previous Section 3, different surrogate strategies are developed in this Section 4. By using them, the computational costly finite element analysis of each local subproblem stated in $D_k(\omega)$ can efficiently be replaced to accelerate

(a) Reference domain $\hat{M}_1$ with circular void

(b) Target domain example based on $\hat{M}_1$

(c) Reference domain $\hat{M}_2$ with elliptical void

(d) Target domain example based on $\hat{M}_2$
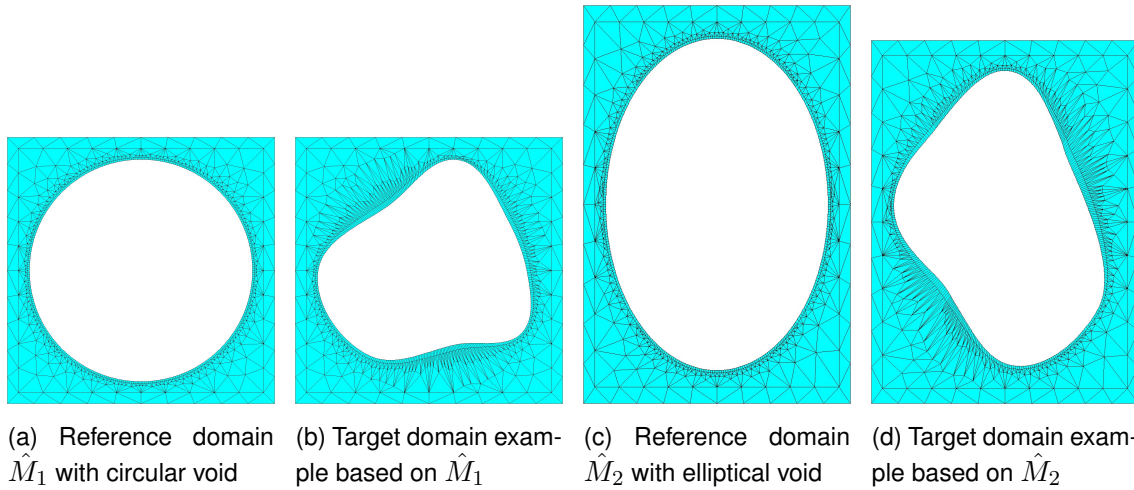
Figure 5: Based on two reference meshes $\hat{M}_\ell$, local subdomains are discretized by construction of Ψ_ℓ. The transformations are non-linear in the inner rectangles $\hat{P}_\ell^{\text{in}}$ and linear in the remaining area $\hat{P}_\ell^{\text{out}} \backslash \hat{P}_\ell^{\text{in}}$ ($\ell = 1, 2$).

the iteration process of the Schwarz alternating method. For a given realization of random voids, this approach can be interpreted as a (multiplicative or additive) Schwarz alternating method with inexact local solutions. The convergence of the discretized and thus algebraic problem then may follow from [2].

4.1   Compressed local solution operator $\mathcal{C}_\ell$

The parameter $\boldsymbol{p}_k \in \Xi_0^\ell$ is given for fixed $\ell = 1, \ldots, L$ as in Section 3.2.3. The fixed discretization of $\hat{\mathcal{M}}_\ell$ implies a parameter dependent linear solution operator $\mathcal{S}_\ell^h(\boldsymbol{p}_k) \approx \mathcal{S}_\ell(\boldsymbol{p}_k)$ of the local problem of fixed shape having a void $P_k(\boldsymbol{p}_k)$. This operator takes the current (interpolated) Dirichlet trace on $\partial P_k^{\text{out}}$ and returns a (interpolated) Dirichlet trace on ∂P_k^{in} with regard to the underlying mesh discretizations of $D_0(\omega)$ and $D_k(\omega)$. Consequently, the input and output are usually mesh size dependent.

Motivated by the regularity of $\boldsymbol{u}(\omega)$ in $D(\omega)$, a mesh independent compression is envisaged. For a continuous function $\boldsymbol{u} \colon P_k^{\text{out}} \to \mathbb{R}^d$ with trace $\operatorname{tr} \boldsymbol{u}$, a continuous piecewise Lagrange polynomial trace interpolation $\mathcal{I}_{\boldsymbol{q}}^\#$, $\# \in \{\text{in,out}\}$ of order $\boldsymbol{q} = (q_1, \ldots, q_{Q_d}) \in \mathbb{N}^{Q_d}$, $Q_d = 4$ and $Q_d = 6$ for $d = 2$ and $d = 3$ respectively, of the form

$$\mathcal{I}_{\boldsymbol{q}}^\#(\operatorname{tr} \boldsymbol{u}) = \text{polynomial of degree } q_i \text{ on the } i\text{-th segment of } \partial P_k^\# \tag{11}$$

is constructed. The segments correspond to edges for $d = 2$ and facettes for $d = 3$.

Let $N_{\boldsymbol{q}}$ denote the degrees of freedom of the interpolation scheme. In case of $\boldsymbol{q} = (q, \ldots, q)$, it holds

$$N_{\boldsymbol{q}} = \begin{cases} 4qd & \text{for } d = 2 \quad (\boldsymbol{u}_x, \boldsymbol{u}_y), \\ 2\left(3q^2 + 1\right)d & \text{for } d = 3 \quad (\boldsymbol{u}_x, \boldsymbol{u}_y, \boldsymbol{u}_z). \end{cases} \tag{12}$$

For a vector $\boldsymbol{c} \in \mathbb{R}^{N_{\boldsymbol{q}}}$, $\mathcal{I}_{\boldsymbol{q}}^\#[\boldsymbol{c}]$ represents the interpolation module of Eq. (11) and defines a function on the boundary $\partial P_k^\#$ with degrees of freedom setted to $\boldsymbol{c}$. Vice versa for given trace $\operatorname{tr} \boldsymbol{u}$, let $\mathcal{I}_{\boldsymbol{q}}^\#[\operatorname{tr} \boldsymbol{u}] \in$

$\mathbb{R}^{N_q}$ be the vector of degrees of freedom $\boldsymbol{c}$. Now allowing for different interpolation order $\boldsymbol{q}^{\#}$ for $\# \in \{$in,out$\}$, the latter constructions imply the following compressed mapping

$$\begin{aligned} \mathcal{C}_\ell : \mathbb{R}^{N_{\boldsymbol{q}^{\mathrm{out}}}} \times \Xi_0^\ell &\rightarrow \mathbb{R}^{N_{\boldsymbol{q}^{\mathrm{in}}}} \\ (\boldsymbol{c}_{\mathrm{out}}, \boldsymbol{p}_k) &\mapsto \boldsymbol{c}_{\mathrm{in}} := \mathcal{C}_\ell(\boldsymbol{c}_{\mathrm{out}}, \boldsymbol{p}_k) = \mathcal{I}_{\boldsymbol{q}^{\mathrm{in}}}^{\mathrm{in}} \left[\mathrm{tr}\left(\mathcal{S}_\ell^h(\boldsymbol{p}_k) \circ \mathcal{I}_{\boldsymbol{q}^{\mathrm{out}}}^{\mathrm{out}}[\boldsymbol{c}_{\mathrm{out}}] \right) \right]. \end{aligned} \tag{13}$$

Using this compressed mapping, a compressed Schwarz alternating method is proposed, summarized in Algorithm 1. The case $N_{\boldsymbol{q}^{\mathrm{out}}} \neq N_{\boldsymbol{q}^{\mathrm{in}}}$ may occur in the case of matching or non-matching meshes.

Algorithm 1 Compressed Schwarz alternating method

Require: $N = N(\omega), \boldsymbol{\xi}(\omega) = \boldsymbol{p} = (\boldsymbol{p}_1, \dots, \boldsymbol{p}_N), \beta_2 > \beta_1 > 0, u_{\mathrm{lim}}$
Ensure: discrete solution $\boldsymbol{u}_h(\omega) \approx \boldsymbol{u}(\omega)$
  $(D_k(\omega))_{k=1}^N \leftarrow$ define subdomains based on $\{\beta_1, \beta_2\}$ as in Fig. 2
  $(\partial P_k^{\#})_{k=1}^N \leftarrow$ define local boundaries for $\# \in \{$in,out$\}$
  $(\mathcal{M}_\ell(\boldsymbol{p}_k))_{k=1}^N \leftarrow$ construct local mesh families using Ψ_ℓ from Section 3.2.3
  $i \leftarrow 0$ initialize iteration number
  $\boldsymbol{u}_{h,0}^i \leftarrow$ initialize random discrete Dirichlet boundary condition on $\partial D_k(\omega), k = 1, \dots, N$
  precompute discrete solution operator $\mathcal{S}_0^h$ on $D_0(\omega)$ based on factorization of stiffness matrix K_0
  while convergence criteria (u_{lim}) not met **do**
    for $k = 1, \dots, N$ in parallel **do**
      compute $\boldsymbol{u}_{h,k}^i$ on $\partial P_k^{\mathrm{in}}$ using $\mathcal{C}_\ell$ from Eq. (13) based on local meshes
    end for
    $i \leftarrow i + 1$
    solve Eqs. (8)–(9) with $\mathcal{S}_0^h$ for $\boldsymbol{u}_{h,0}^i$ on $D_0(\omega)$ using traces $\mathrm{tr}\, \boldsymbol{u}_{h,k}^{i-1}$ on $(\partial P_k^{\mathrm{in}})_{k=1}^N$
    compute traces $\mathrm{tr}\, \boldsymbol{u}_{h,0}^i$ on $(\partial P_k^{\mathrm{out}})_{k=1}^N$
  end while
compute $\boldsymbol{u}_h(\omega) = (\boldsymbol{u}_{h,k}^i)_{k=1}^N$ based on converged Dirichlet traces

---

4.2 Surrogate design

The evaluation of the compressed operators $\mathcal{C}_\ell$ in Algorithm 1 still involves the approximate solution of a local PDE system in $D_k(\omega)$ in each iteration step. The structure of $\mathcal{C}_\ell$ is used to propose a suitable surrogate to replace this rather expensive step. Note that it is possible to accelerate the sampling process only with a finite number $\ell = 1, \dots L$ of surrogates, since FEM computations have to be performed only on the coarse domain $D_0(\omega)$ per sample. In particular no meshing and local FEM computation associated to the voids is necessary in the online phase of computation.

It has been observed first that $\boldsymbol{c}_{\mathrm{out}} \mapsto \mathcal{C}_\ell(\boldsymbol{c}_{\mathrm{out}}, \boldsymbol{p}_k)$ is a linear map for fixed $\boldsymbol{p}_k \in \Xi_\ell$ and $\boldsymbol{f} \equiv 0$. It is composed of a linear solution operator and linear interpolation operators. Consequently, this map can be interpreted as a matrix-valued function

$$\boldsymbol{C}_\ell : \Xi_\ell \ni \boldsymbol{p}_k \mapsto \boldsymbol{C}_\ell(\boldsymbol{p}_k) \in \mathbb{R}^{N_{\boldsymbol{q}^{\mathrm{out}}}, N_{\boldsymbol{q}^{\mathrm{in}}}}. \tag{14}$$

Based on the size of $\boldsymbol{p}_k, N_{\boldsymbol{q}^{\mathrm{out}}}, N_{\boldsymbol{q}^{\mathrm{in}}}$ and the linear substructure, the design of the surrogate can be defined. Note that the evaluation of $\boldsymbol{C}_\ell(\boldsymbol{p}_k)$ can be realized in parallel by solving $N_{\boldsymbol{q}^{\mathrm{out}}}$ local Dirichlet problems with associated interpolation degree of freedom vectors $\boldsymbol{c}_{\mathrm{out}} = \epsilon \boldsymbol{e}_m$ for some $\epsilon > 0$ and unit vector $\boldsymbol{e}_m$ for $m = 1, \dots, N_q$, see Fig. 6.

(a) $\boldsymbol{u}_x$ for $\boldsymbol{c}_{\text{out}} = \epsilon \boldsymbol{e}_1$

(b) $\boldsymbol{u}_y$ for $\boldsymbol{c}_{\text{out}} = \epsilon \boldsymbol{e}_1$

(c) $\boldsymbol{u}_x$ for $\boldsymbol{c}_{\text{out}} = \epsilon \boldsymbol{e}_{32}$

(d) $\boldsymbol{u}_y$ for $\boldsymbol{c}_{\text{out}} = \epsilon \boldsymbol{e}_{32}$
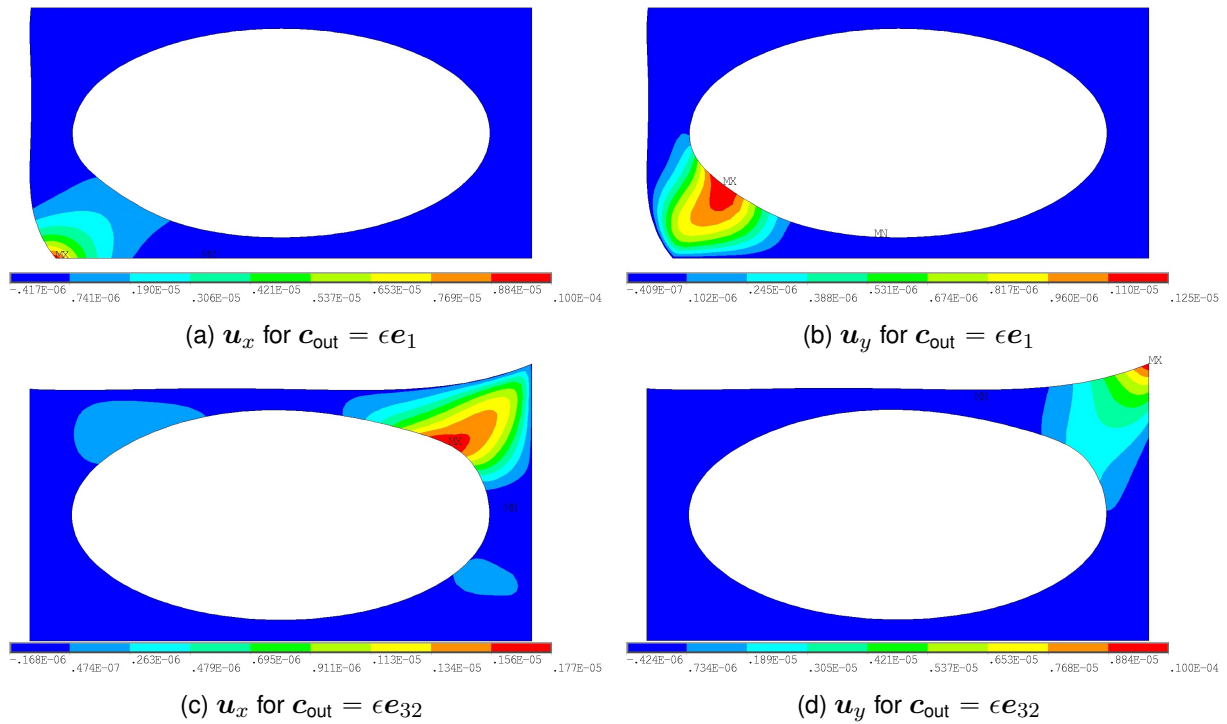
Figure 6: Displacement field $\boldsymbol{u} = (\boldsymbol{u}_x, \boldsymbol{u}_y)$ in the local subdomain with an elliptical void $P_k(\boldsymbol{p}_k)$ for certain scaled unit vectors ϵe_m with $\epsilon = 10^{-5}$, $\boldsymbol{q}^{\text{out}} = (4, 4, 4, 4)$ and $d = 2$.

4.2.1 Surrogate for elliptical or ellipsoidal voids

An elliptical in $d = 2$ or an ellipsoidal void in $d = 3$ is denoted as P_k and can be parametrized by its midpoint and radii $r_1, \ldots, r_d$. Due to the isotropic behavior of the underlying material in Eq. (2), the local parameterization can be restricted to the radii only. Furthermore, recall the fixed choice of $\{\beta_1, \beta_2\}$ and the corresponding relative fixed structures $\{P_k^{\text{in}}, P_k^{\text{out}}\}$. Then the mapping $\boldsymbol{C}_\ell(\cdot, \boldsymbol{c}_{\text{out}})$ from Eq. (13) for fixed $\boldsymbol{c}_{\text{out}}$ associated to radii parameterization only changes its values if the ratios of radii $\rho = r_2/r_1$ for $d = 2$ or $\rho_{21} = r_2/r_1$ and $\rho_{31} = r_3/r_1$ for $d = 3$ change. The parameterization of an elliptical/ ellipsoidal void can consequently be reduced to $\boldsymbol{p}_k = \rho$ for $d = 2$ or $\boldsymbol{p}_k = (\rho_{21}, \rho_{31})$ for $d = 3$. Due to the expected smoothness of the matrix-valued mapping $\boldsymbol{p}_k \mapsto \boldsymbol{C}_\ell$ for $\boldsymbol{p}_k \in \Xi_0^\ell$, the surrogate takes the form of a Chebyshev interpolation

$$\boldsymbol{C}_\ell(\boldsymbol{p}_k) \approx \sum_{\alpha \in \Lambda} \boldsymbol{C}_\alpha T_\alpha(\boldsymbol{p}_k) \tag{15}$$

with (tensorized) Chebyshev polynomials $(T_\alpha)_{\alpha \in \Lambda}$, matrix-valued coefficients $(\boldsymbol{C}_\alpha)_{\alpha \in \Lambda}$ and index set $\Lambda \subset \mathbb{N}^{d-1}$.

4.2.2 Surrogate for star-shaped voids for $d = 2$

The parameter $\boldsymbol{p}_k \in \Xi_k \subset \Xi_0 \subset \mathbb{R}^{M_k}$ has to be considered in case of arbitrarily shaped voids. As M_k gets large, the use of tensorized surrogate schemes gets limited by the curse of dimensionality. The surrogate class of choice is an artificial neural network (ANN). Based on the underlying structure of $\mathcal{C}_\ell$, it is necessary to learn a surrogate either with $(M_k + N_{\boldsymbol{q}^{\text{out}}})$-dimensional input and $N_{\boldsymbol{q}^{\text{in}}}$-dimensional output or with M_k-dimensional input and $(N_{\boldsymbol{q}^{\text{out}}} \times N_{\boldsymbol{q}^{\text{in}}})$-dimensional output. Note that the first mentioned input output relation is needed in case of $\mathcal{C}_\ell$ being non-linear in both input parameters. In what

follows the matrix valued case is utilized. The star-shaped voids may also be parametrized only by radii ratios $\rho_{i1} = r_i/r_1$ with regard to θ_i with $i = 2, \ldots, M_k$, using the same argument as in Section 4.2.1. The radial component r_1 for θ_1 is fixed, which reduces again the number of initial parameters by one. Consequently, a star-shaped void is encoded in the parameter $\boldsymbol{p}_k = (\rho_{i1})_{i=2}^{M_k}$ yielding the surrogate approach

$$C_\ell(\boldsymbol{p}_k) \approx \mathsf{ANN}(\boldsymbol{p}_k). \tag{16}$$

The actual structure of the used ANN is discussed in Section 5.2.

5 Applications

In the following, three different models according to Section 2 are presented to demonstrate the applicability and usefulness of the developed surrogate model strategies. In Section 5.1, a two-dimensional plate perforated by elliptical voids is investigated. The application on the holed domain of Fig. 1a with a mixture of circular, elliptical and arbitrarily shaped voids is shown in Section 5.2. A three-dimensional problem is given in Section 5.3, where the numerical predictions are validated by experimentally measured strains.

5.1 Application 1: elliptical voids in a 2D plate

In Fig. 7a, a sample of a holed two-dimensional domain D with $N = 20$ elliptical voids is shown. The radii ratios $\boldsymbol{p}_k = \rho$ are given as $\{3/2, 2/3, 1.0, 2/5, 5/2\}$ and the voids are quadrupled in vertical direction. The domain is loaded in horizontal direction on the right and fixed on the left. The resulting displacement fields $(\boldsymbol{u}_x, \boldsymbol{u}_y)$ and the maximum first/ minimum third principal stress on kth void $(\sigma_{1,\max}, \sigma_{3,\min})_k$ are given in Fig. 7b–7d.

Based on the proposed Schwarz alternating method with local surrogate responses from Section 3.1 and 4, the two-scale model in Fig. 8a has been developed. The skeletal domain D_0 with N rectangular holes $P_k^\#$ and N subdomains D_k, each one with an elliptical void P_k inside, are coupled by an overlapping area based on relative values $\{\beta_1, \beta_2\} = \{0.10, 0.20\}$, see Fig. 8a. The domain is extremely simplified and consists only of 14326 degrees of freedom (instead of 105150 degrees of freedom in the one-scale model). Furthermore, the system stiffness matrix K_0 associated with D_0 is assembled only once and factorized at the beginning of the solution process. During the iteration, the Dirichlet boundary values $\boldsymbol{u}_k$ on $\partial P_k^{\mathrm{in}}$ are successively replaced until convergence. Convergence is given if the deviation of the Dirichlet trace to the reference solution of the one-scale model is smaller than a defined threshold of $u_{\lim} = 10^{-2}$, that means if

$$\frac{\|\boldsymbol{u}_{d,k,i} - \boldsymbol{u}_{d,k,\mathrm{ref}}\|}{\|\boldsymbol{u}_{d,k,\mathrm{ref}}\|} < u_{\lim} = 10^{-2} \qquad \forall d = \{x, y\} \text{ and } \forall k = \{1, \ldots, N\}. \tag{17}$$

The subdomains of the two-scale model are solved by using the surrogate model from Section 4.2.1 based on decomposed ratio input domain $\Xi_0 = [1,2] \cup [2,3] \cup [3,4] \cup [4,5]$ using Chebyshev polynomials with $\Lambda = \{0, \ldots, 4\}$ and a compression degree of $\boldsymbol{q} = \boldsymbol{q}^{\mathsf{in}} = \boldsymbol{q}^{\mathsf{out}}$. The resulting accuracy of the surrogate is shown in Table 1.

The horizontal and vertical displacement fields are shown in Fig. 8b–8c in D_0. Converged Dirichlet boundary values $\boldsymbol{u}_k$ on $\partial P_k^{\mathrm{in}}$ for each void lead to same displacement values in the overall domain. The deviations of the principal stresses $(\sigma_{1,\max}, \sigma_{3,\min})_k$ on the voids to the solutions of the one-scale

(a) Holed domain D

(b) Stress values $(\sigma_{1,\mathrm{max}}, \sigma_{3,\mathrm{min}})_k$ on voids

(c) Horizontal displacement field $\boldsymbol{u}_x\,[\mathrm{m}]$

(d) Vertical displacement field $\boldsymbol{u}_y\,[\mathrm{m}]$
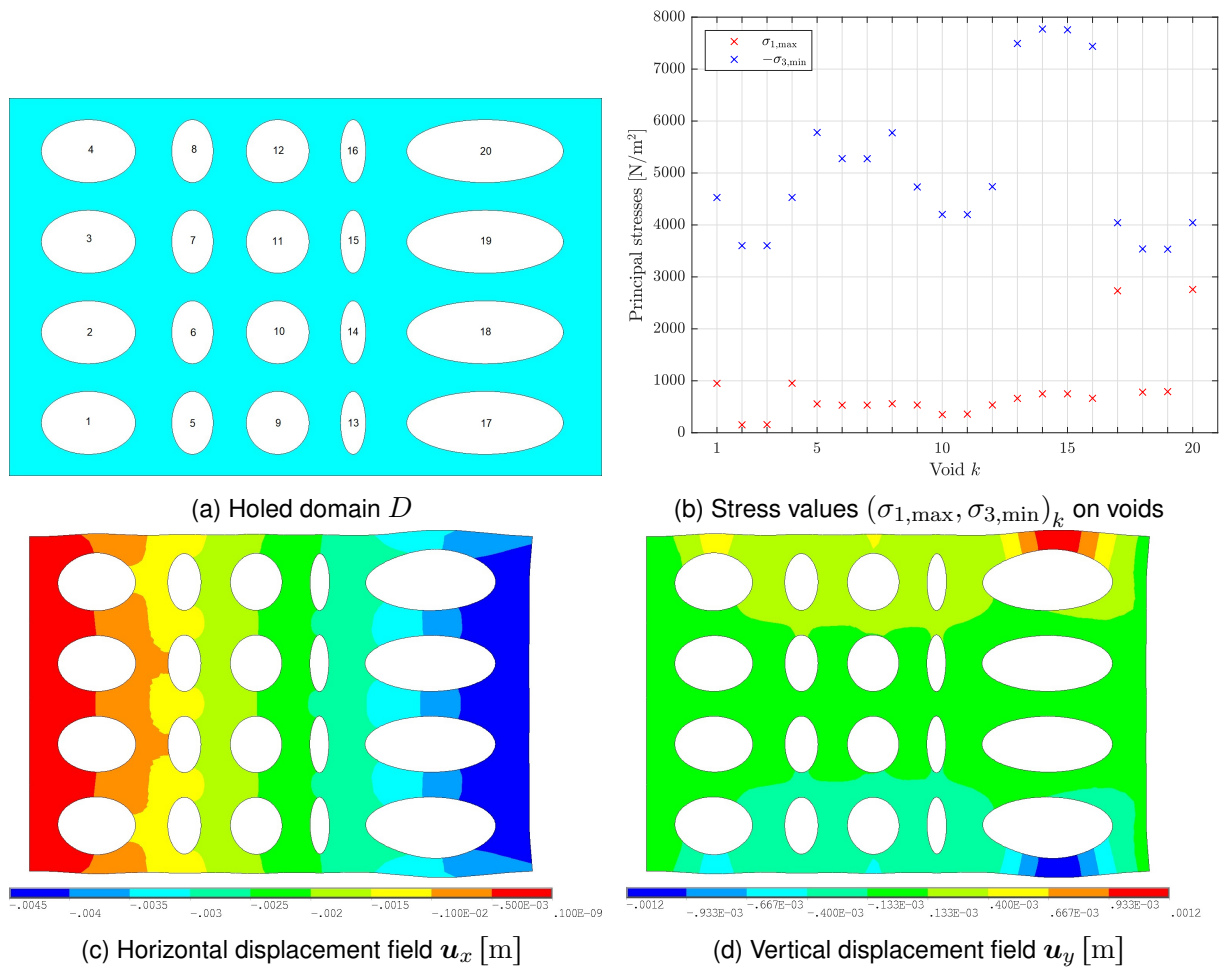
Figure 7: Holed 2D domain and quantities of interest by solving the one-scale model.

Table 1: Chebychef interpolation quality regarding $\rho \to \|\|\boldsymbol{C}(\rho)_\ell\|_{\mathrm{F}}\|_\infty$.

domain	$\boldsymbol{q} = (2,2,2,2)$	$\boldsymbol{q} = (10,10,10,10)$	$\boldsymbol{q} = (21,21,21,21)$
$[1,2]$	$8.7 \cdot 10^{-6}$	$1.3 \cdot 10^{-5}$	$4.2 \cdot 10^{-5}$
$[2,3]$	$4.4 \cdot 10^{-6}$	$5.7 \cdot 10^{-6}$	$6.1 \cdot 10^{-6}$
$[3,4]$	$2.9 \cdot 10^{-6}$	$2.3 \cdot 10^{-6}$	$5.4 \cdot 10^{-6}$
$[4,5]$	$2.3 \cdot 10^{-6}$	$4.1 \cdot 10^{-6}$	$6.3 \cdot 10^{-6}$

model are shown in Fig. 8d. The maximum deviation of around 1% can be detected for the maximum first principal stress on void 7. A smaller value of u_{lim} would decrease the deviations toward zero during the Schwarz alternating method.

5.2 Application 2: arbitrarily shaped voids in a 2D plate

The extension to arbitrarily shaped voids is shown in this Section 5.2. The underlying holed domain of Fig. 1a consists of one circular, one rotated elliptical and three arbitrarily shaped voids. For the two first mentioned shapes, the surrogate model from Section 4.2.1 is used again. For the latter ones, the surrogate model from Section 4.2.2 is used with different values of the compression degree $\boldsymbol{q} = \boldsymbol{q}^{\mathrm{in}} =$

(a) Domain D_0 and one subdomain D_1

(b) Deviation to Fig. 7b: $(\Delta\sigma_{1,\mathrm{max}}, \Delta\sigma_{3,\mathrm{min}})_k$

(c) Horizontal displacement field $\boldsymbol{u}_x\,[\mathrm{m}]$

(d) Vertical displacement field $\boldsymbol{u}_y\,[\mathrm{m}]$
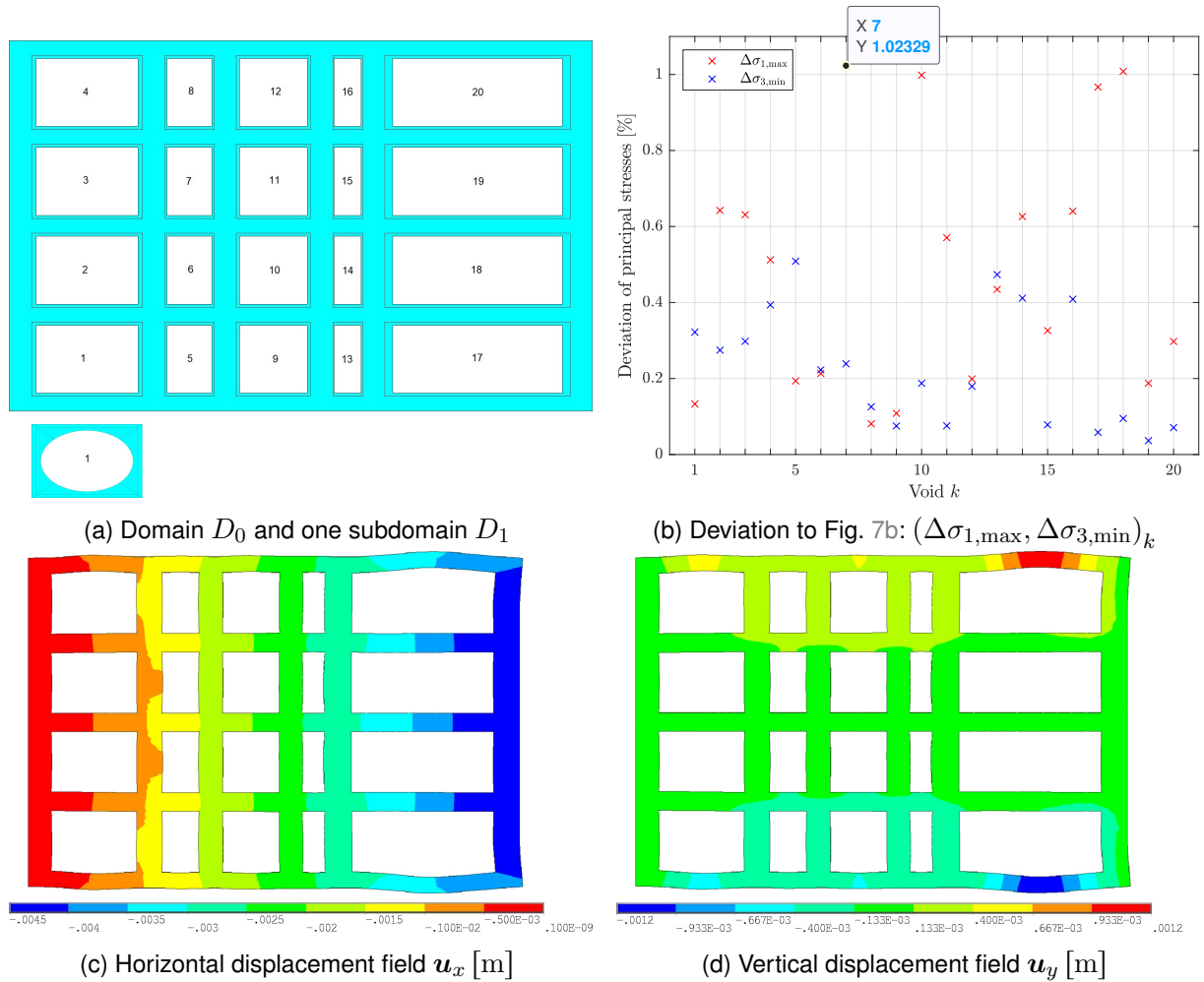
Figure 8: Two-scale model and deviations to the quantities of interest achieved by solving the one-scale model.

$\boldsymbol{q}^{\mathrm{out}}$. For all ANNs, the Huber loss function with varying values for δ_{Huber} serves as objective function. The hyperband algorithm [21] and a following grid search [12] leads to "optimal" ANN parameters, some of them are given in Table 2. The quality of the individual ANNs is reflected by the training and validation loss values. It is worth mentioning, that the ANN dimension increases by higher $\boldsymbol{q}$ values leading to higher loss values in the underlying problem. The displacement fields $\boldsymbol{u}_x$ and $\boldsymbol{u}_y$ are depicted in Fig. 9, by solving both the one-scale model and the two-scale model. Due to the convergence of the Dirichlet boundary values $\boldsymbol{u}_k$ on $\partial P_k^{\mathrm{in}}$, the displacement values in the overall domain D_0 matches the displacement values of the one-scale model quite well. Finally, the stress values $(\sigma_{1,\mathrm{max}}, \sigma_{3,\mathrm{min}})_k$ on each void and the relative deviations are listed in Table 3. The deviations are as well very small depending on the defined threshold of $u_{\mathrm{lim}} = 10^{-2}$ for convergence during the Schwarz alternating method.

5.3   Application 3: comparison with experimentally measured strains

Investigating adhesive bonds for rotor blades of wind turbines is usually conducted on special representative sub-components. One of them is called the Henkel beam (HB), developed by the Fraunhofer Institute for Wind Energy and Energy System Technology (IWES) within the european UpWind-

Table 2: Some determined "optimal" ANN parameters and ANN quality values.

parameter	$\boldsymbol{q} = (2, 2, 2, 2)$	$\boldsymbol{q} = (10, 10, 10, 10)$	$\boldsymbol{q} = (21, 21, 21, 21)$
δ_{Huber}	0.01	0.01	0.01
layers	4	4	2
neurons per layer	128→2048→2048→256	512→1024→2048→1024	512→512
activation function	relu	swish	relu
dropoutrate	0.0	0.2	0.3
optimizer	adam	RMSprop	adam
training loss	$6.8 \cdot 10^{-4}$	$8.6 \cdot 10^{-4}$	$6.5 \cdot 10^{-3}$
validation loss	$6.7 \cdot 10^{-5}$	$5.6 \cdot 10^{-4}$	$6.6 \cdot 10^{-3}$

(a) Horizontal displacement field $\boldsymbol{u}_x \, [\mathrm{m}]$

(b) Vertical displacement field $\boldsymbol{u}_y \, [\mathrm{m}]$
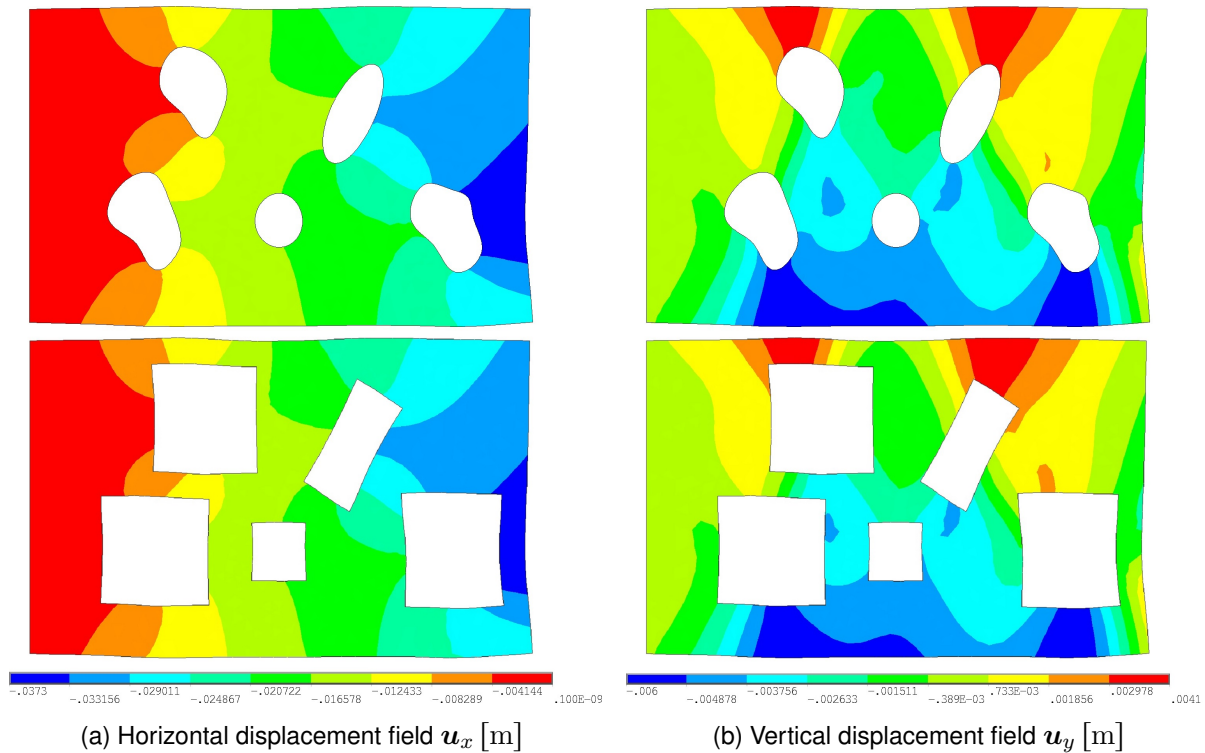
Figure 9: Displacement fields either by solving the one-scale or the two-scale model.

project [24]. Extensive experimental and numerical studies have been conducted inhouse by the authors and former employees, see [22, 18, 7, 6, 20, 8, 9]. The Henkel beam is a three-dimensional composite structure with reinforcements near the fixations on the left and near the load application point on the right, see Fig. 10a. The upper adhesive bond (Fig. 10b) between the upper flange and the web is defined as the bond of interest in the unreinforced region between $[570, 1320]$ mm. Applying a vertical load leads to axial strains ϵ_x in the bond which matches the theoretical solution quite well in the case of a perfect bond, see Fig. 10c. In the presence of inaccuracies and imperfections, which typically appear during the manufacturing process of adhesive bonds in rotor blades, the measured axial strains differ from the theoretical solution. In one Henkel beam (HB10), four relatively large imperfections have been included in advance within the region of $[690, 890]$ mm and have been scanned by a computer tomographic device, see Fig. 10d. For simplification purposes, the air voids are approximated by ellipsoids without rotation ($\phi_{k,x/y/z} = 0°$) in the following. The remaining parameters

Table 3: Stress values $(\sigma_{1,\max}, \sigma_{3,\min})_k$ $[\mathrm{N/m^2}]$ on each void.

void	one-scale model		two-scale model (relative deviation in brackets)	
k	$\sigma_{1,\max}$	$\sigma_{3,\min}$	$\sigma_{1,\max}$	$\sigma_{3,\min}$
1	1295	-6100	$1295\,(\pm 0.00\%)$	$-6121\,(+0.34\%)$
2	1575	-6997	$1568\,(-0.44\%)$	$-6996\,(-0.01\%)$
3	2762	-5953	$2767\,(+0.18\%)$	$-5966\,(+0.22\%)$
4	1179	-4169	$1175\,(-0.34\%)$	$-4172\,(+0.07\%)$
5	1877	-6237	$1877\,(\pm 0.00\%)$	$-6223\,(-0.22\%)$
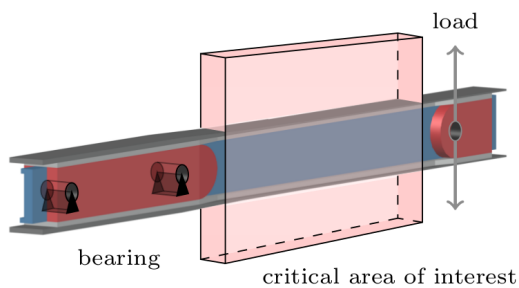
(a) Henkel beam model
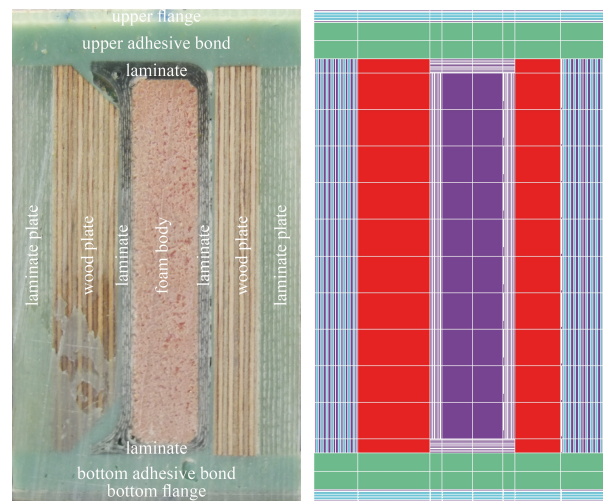
(b) Cross-section in the reinforced region
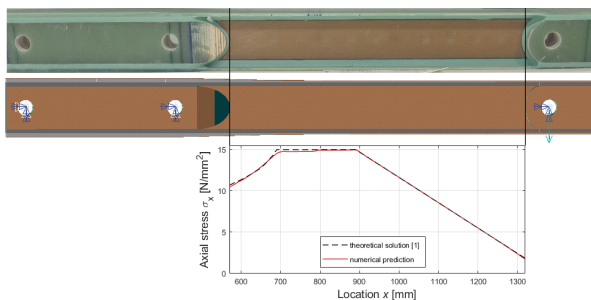
(c) Axial stress σ_x in the adhesive bond without imperfections
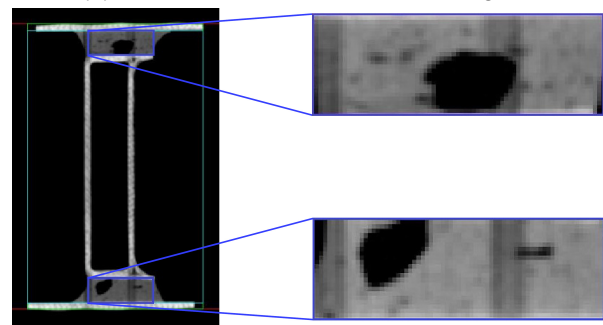
(d) CT scan for air void detection

Figure 10: The Henkel beam as an example for a real engineering problem. The focus is on axial strains ϵ_x in the upper adhesive bond.

are listed in Table 4. The experimentally measured axial strains ϵ_x and their numerical predictions are compared in Fig. 11. The numerical predictions results from the one-scale model and the two-scale model in which the surrogate model from Section 4.2.1 (using Chebyshev polynomials by degree 4 for each radii ratio) is applied for the four subdomains.

The numerically predicted axial strains are higher on average than the experimentally determined values. In the numerical models, the strain has been evaluated directly on the upper boundary of

Table 4: Air void properties (approximated by ellipsoids with $\phi_{k,x/y/z} = 0°$ for simplification).

air void	midpoint coordinates [mm]			radii [mm]		
k	$m_{k,x}$	$m_{k,y}$	$m_{k,z}$	$r_{k,x}$	$r_{k,y}$	$r_{k,z}$
1	692.5	5.0	11.6	23.6	3.9	9.4
2	783.3	5.0	11.6	15.6	2.1	8.6
3	831.2	5.0	11.6	8.8	2.4	8.3
4	855.2	5.0	11.6	8.4	3.9	6.5
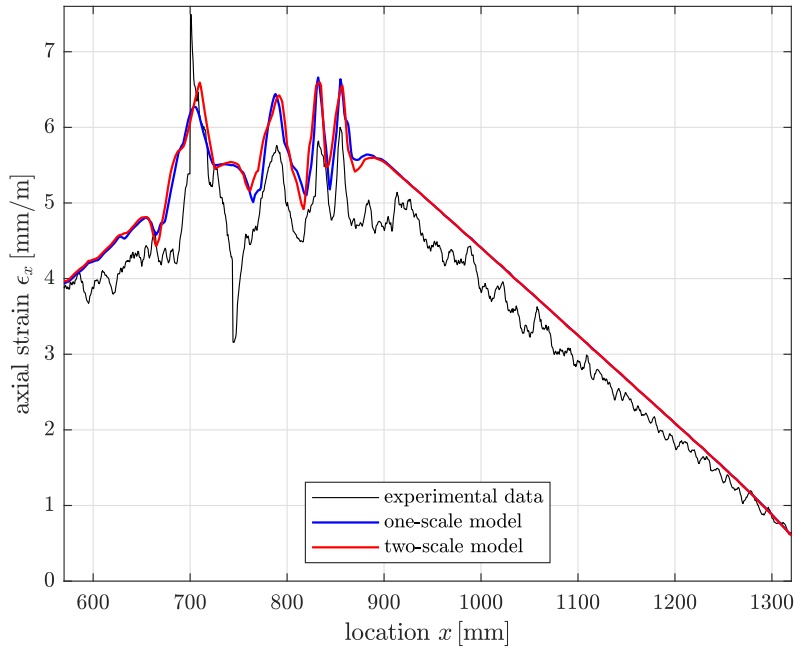
Figure 11: Axial strain ϵ_x in the upper adhesive bond in the critical area of interest between $[570, 1320]$ mm.

the adhesive bond what could not been enabled in the conducted real experiments. The fiber-optic sensors have been installed as near as possible on the upper boundary, but with an offset toward inside. The imperfections lead to higher axial strains which could be determined both experimentally and numerically. The location of the four large imperfections could be detected perfectly. The measured and predicted strain values near the air voids differ by a maximum of 20%. Reasons could be the simplification to ellipsoids without rotation in the numerical prediction as well as inaccuracies in the conducted measurements. Nevertheless, the axial strains predicted by the one-scale and by the two-scale model are very similar which validates the developed method in the numerical sense for the three-dimensional case.

6 Conclusions and outlook

A new developed surrogate model using an overlapping domain decomposition scheme based on Schwarz alternating method is presented in this contribution. The developed approach is applied on different two- and three-dimensional problems and finally also compared to experimentally determined structural responses. By using this method, it is possible to efficiently predict the local structural behavior with associated values like displacements, strains and stresses. The computational costly numerical analyses of holed subdomains are replaced by appropriate surrogate models leading to an acceleration compared to the classical Schwarz alternating method. In particular the workload in one iteration step effectively depends on the forward-backward solving of the factorized stiffness matrix $K_0(\omega)$ associated to $D_0(\omega)$, since in comparison the effort of surrogate based responses of local subproblems can be neglected. The introduction of simple surrounding geometries, denoted as P_k^{out} within this work, and the possibility to apply non-matching meshes between overlapping subdomains allows for simpler and coarser meshing of $D_0(\omega)$. This in turn renders a comparable low cost computational model per iteration step. The application is beneficial if a high amount of very small and closely positioned voids with complicated shapes would extremely increase the complexity of a corresponding one-scale model.

The solution of the local subproblem are displacement values depending on two input parameters, whose influence is separable: the shape of the included void and the present Dirichlet values on the boundary of the subproblem. The shape of the included void can be parametrized in normalized form (the smallest parameter is set to 1) leading to a reduction of the dimension by one. For elliptical and ellipsoidal voids, the resulting parameter space can efficiently be interpolated by (tensorized) Chebyshev polynomials with a small polynomial degree of 4. The parameter space is higher dimensional for arbitrarily shaped voids for which a surrogate model based on ANN has successfully been constructed. The mapping of the present Dirichlet values on the boundary of the subproblem on the solution values is determined as linear. A compressed mapping is investigated in which interpolations using Lagrange polynomials are used, separated according to the underlying Dirichlet value and the submodel boundary. The deviation of the interpolation to the displacement on the boundary has to be small enough to ensure convergence in the compressed Schwarz alternating method. An adaptive approach is implemented which determines the necessary polynomial degree of the underlying Lagrange polynomials.

The presented concept can be extended in multiple directions. First, the chosen design of the surrogates has relied on the linearity of the compression operator C_ℓ which has resulted from the linearity of the underlying solution operator of the local subproblems. Thus the extension to non-linear partial differential equations would require surrogate responses of the form $\mathbb{R}^{N_{q^{\text{in}}},M_k} \to \mathbb{R}^{N_{q^{\text{out}}}}$. Second, the compression of the degrees of freedom associated to the Dirichlet-to-Dirichlet relation has been realized by Lagrange interpolation. More advanced reduction techniques such as reduced basis projections could be applied. Note that one deals with functions on the transmission interface only. In particular they may have limited dependence on the multiscale behavior of the solution close to the voids, if the distance of voids and their surrounding domain boundary gets bigger. Third, the extension to deterministic anisotropic materials would require the inclusion of a parameterization of P_k^{out} to the input space of the surrogates. In this work, fixed relative values β_1, β_2 have been defined which are redundant in the isotropic case. Finally, for sake of simplicity, this work has relied on the classical Schwarz alternating method based on Dirichlet-to-Dirichlet transmission conditions, which cause slow convergence speed in cases of small overlapping domains. The presented techniques can also be formulated in the framework of optimized Schwarz alternating methods [14] to improve the convergence rate during the iterative solution process.

References

[1] Ted L. Anderson. *Fracture mechanics - fundamentals and applications*. CRC Press, Boca Raton, 2017.

[2] Michele Benzi, Andreas Frommer, Reinhard Nabben, and Daniel B Szyld. Algebraic theory of multiplicative Schwarz methods. *Numerische Mathematik*, 89(4):605–639, 2001.

[3] Eric T. Chung, Yalchin Efendiev, Guanglian Li, and Maria Vasilyeva. Generalized multiscale finite element methods for problems in perforated heterogeneous domains. *Applicable Analysis*, 95(10):2254–2279, 2016.

[4] Eric T. Chung, Maria Vasilyeva, and Yating Wang. A conservative local multiscale model reduction technique for stokes flows in heterogeneous perforated domains. *Journal of Computational and Applied Mathematics*, 321:389–405, 2017.

[5] Andres A. Contreras, Paul Mycek, Olivier P. Le Maître, Francesco Rizzi, Bert Debusschere, and Omar M. Knio. Parallel domain decomposition strategies for stochastic elliptic equations part b: accelerated monte carlo sampling with local pc expansions. *SIAM Journal on Scientific Computing*, 40(4):C547–C580, 2018.

[6] Martin Drieschner, Robert Gruhlke, Yuri Petryna, Martin Eigel, and Dietmar Hömberg. Analysis of model and data uncertainties for the failure of adhesive bonds in composite materials. *PAMM*, 20(1):e202000081, 2021.

[7] Martin Drieschner, Hermann G. Matthies, Truong-Vinh Hoang, Bojana V. Rosić, Tim Ricken, Carla Henning, Georg-Peter Ostermeyer, Michael Müller, Stephan Brumme, Tarin Srisupattarawanit, Kerstin Weinberg, and Tim F. Korzeniowski. Analysis of polymorphic data uncertainties in engineering applications. *GAMM-Mitteilungen*, 42(2):e201900010, 2019.

[8] Martin Drieschner and Yuri Petryna. Acquisition of polymorphic uncertain data based on computer tomographic scans and integration in numerical models of adhesive bonds. Preprint Technische Universität Berlin, 2019.

[9] Martin Drieschner, Yuri Petryna, and Lukas Eichner. Parameterization of arbitrary hole shapes using non-destructive testing and resulting stress concentration in a 2d plate with finite dimensions. Preprint Technische Universität Berlin, 2019.

[10] Martin Drieschner, Yuri Petryna, Robert Gruhlke, Martin Eigel, and Dietmar Hömberg. Comparison of various uncertainty models with experimental investigations regarding the failure of plates with holes. *Reliability Engineering & System Safety*, 203:107106, 2020.

[11] Martin Eigel and Robert Gruhlke. A local hybrid surrogate-based finite element tearing interconnecting dual-primal method for nonsmooth random partial differential equations. *International Journal for Numerical Methods in Engineering*, 122(4):1001–1030, 2021.

[12] Gamze E. Erten, Sinem B. Keser, and Mahmut Yavuz. Grid search optimised artificial neural network for open stope stability prediction. *International Journal of Mining, Reclamation and Environment*, 35(8):600–617, 2021.

[13] Priscilla C. Fonseca and George W. Scherer. An image analysis procedure to quantify the air void system of mortar and concrete. *Materials and Structures*, 48(10):3087–3098, 2015.

[14] Martin J. Gander. Optimized Schwarz methods. *SIAM Journal on Numerical Analysis*, 44(2):699–731, 2006.

[15] Simin He, Youyi Wen, Wenjun Yu, Hong Liu, Cheng Yue, and Jing Bao. Study on voids of epoxy matrix composites sandwich structure parts. *IOP Conference Series: Materials Science and Engineering*, 182:012031, 03 2017.

[16] Poologanathan Keerthan and Mahen Mahendran. Experimental studies of the shear behaviour and strength of lipped channel beams with web openings. *Thin-Walled Structures*, 73:131–144, 2013.

[17] Tim Korzeniowski and Kerstin Weinberg. A markov chain approach to damage evolution in die-cast ZAMAK. *Technische Mechanik*, 38(2):135–147, 2018.

[18] Dragan Kovačević, Yuri Petryna, and Mira Petronijević. Assessment of the impact of air voids on adhesive joints in rotor blades by use of NDT and FEA. pages 3061–3069. 8th European Workshop on Structural Health Monitoring (EWSHM 2016), Vol. 4, 2016.

[19] Murali J. Krishnan and Vitali R. Rengaraju. Air voids reduction phenomena of asphalt concrete – a continuum approach. *International Journal of Fracture*, 97(1/4):337–354, 1999.

[20] Andreas Künzel. *Parameteridentifikation auf Basis faseroptisch gemessener quasi-kontinuierlicher Dehnungssignale*. Doctoral Thesis, Technische Universität Berlin, Berlin, 2016.

[21] Lisha Li, Kevin Jamieson, Giulia DeSalvo, Afshin Rostamizadeh, and Ameet Talwalkar. Hyperband: A novel bandit-based approach to hyperparameter optimization. *Journal of Machine Learning Research*, 18(185):1–52, 2018.

[22] Yuri Petryna, Andreas Künzel, Matthias Kannenberg, Volker Trappe, Dustin Nielow, Daniel Kreutzer, and Stefan Krause. Automatisiertes Verfahren für serienmäßige Integritätsprüfung von Rotorblättern und Bereitstellung von Rotorblatt-Tunern: Verbundprojekt BladeTester: Abschlussbericht: 2011–2015, Abschlussbericht BladeTester, Blade-Tester - Automated approach for serial integrity tests of rotor blades and supply of rotor blade tuners. Technical report, Technische Universität Berlin, Fachgebiet Statik und Dynamik, Berlin, 2015.

[23] Walter D. Pilkey and Deborah F. Pilkey. *Peterson's stress concentration factors, Third Edition*. John Wiley & Sons, Ltd, 2007.

[24] Florian Sayer, Alexandros Antoniou, and Arnoldus van Wingerde. Investigation of structural bond lines in wind turbine blades by sub-component tests. *International Journal of Adhesion and Adhesives*, 37:129–135, 2012. Special Issue on Joint Design 3.

[25] Hermann A. Schwarz. Ueber einen Grenzübergang durch alternirendes Verfahren. *Vierteljahresschrift der Naturforschenden Gesellschaft in Zürich*, 15:272–286, 1870.

[26] Andrea Toselli and Olof Widlund. *Domain decomposition methods - algorithms and theory*. Springer Berlin Heidelberg, Berlin, Heidelberg, 2005.

[27] Zhao Yingjiang, Yan Renjun, and Wang Hongxu. Experimental and numerical investigations on plate girders with perforated web under axial compression and bending moment. *Thin-Walled Structures*, 97:199–206, 2015.

[28] Alan T. Zehnder. *Fracture mechanics*. Springer Berlin Heidelberg, Berlin, Heidelberg, 2012.